

the cold seep sites (Fig. 2A), which may be attributed to the formation of microcracks in the fracture zone of the active fault (19), support the hypothesis that the splay fault is one of the major active faults in the Nankai subduction zone. Slip on the active splay fault may be an important mechanism that accommodates elastic strain due to relative plate motion.

All of the interseismic elastic strain at the updip portion of the seismogenic zone could be released by the coseismic splay fault slip alone, but it seems more likely that there would be slip partitioning between it and the subduction zone (Fig. 3). The splay fault's initial branching portion (Figs. 1 and 2) is within the 1944 Tonankai coseismic rupture area, suggesting a causal relation between the earthquake and slip partitioning. Even though we cannot distinguish the splay fault slip from the subduction zone slip, the splay fault may be responsible for tsunami earthquake generation, accompanying deformation of the forearc accretionary wedge.

The updip limit of the seismogenic zone is constrained by the structural extent of the splay fault and the outer ridge topography, which we believe accumulated during repeated earthquake cycles. Namely, the splay fault's intersection portion with the megathrust (Fig. 3), to which the 1944 coseismic rupture propagated, can be regarded as the "true" updip limit of the seismogenic zone to generate large earthquakes along the subduction zone. Based on thermal modeling (20), the temperature at the true updip limit corresponds to  $\sim 200^\circ\text{C}$ , which is greater than the  $\sim 150^\circ\text{C}$  threshold temperature proposed as the onset of stick-slip behavior (20). The  $\sim 150^\circ\text{C}$  temperature corresponds to the temperature at a portion where the décollement steps down to the top of the oceanic crust under the outer ridge (Figs. 2A and 3).

Finally, structural features such as the décollement stepdown ( $150^\circ\text{C}$  at  $\sim 30$  km) and the splay fault branching ( $200^\circ\text{C}$  at  $\sim 55$  km) enable us to divide the updip portion of the Nankai subducting plate boundary into three different zones (Fig. 3): (i) a decoupled aseismic zone, (ii) a slip partitioning transition zone, and (iii) a coupled seismic zone. For the decoupled aseismic zone between the trough axis (0 km) and the outer ridge,  $\sim 30$  km landward from the trough axis, the presence of stably sliding clays leads to free slip along the décollement (21). Underneath the outer ridge, the décollement steps down to the top of the oceanic crust (Fig. 2A) and the incipient plate-boundary coupling (locking) occurs because of dehydration of clay minerals (21), indicating the onset of interplate stick-slip and seismogenic behavior. The plate-boundary coupling may mature landward in the slip partitioning zone between the décollement stepdown portion and the splay fault branching portion, which can be treated as a transition zone from aseismic to seismic behavior. The splay fault is in the transition zone

and may partition some slip to the surface, where it can help generate a tsunami. The branching portion of the splay fault in the seismic zone is coupled to the subduction zone and may help generate large earthquakes along the plate boundary.

#### References and Notes

1. B. W. Tichelaar, L. J. Ruff, *J. Geophys. Res.* **98**, 2017 (1993).
2. Y. Fukao, *J. Geophys. Res.* **84**, 2303 (1979).
3. T. Kato, *Tectonophysics* **96**, 31 (1983).
4. J.-O. Park et al., *Geophys. Res. Lett.* **27**, 1033 (2000).
5. P. R. Cummins, T. Hori, Y. Kaneda, *Earth Planets Space* **53**, 243 (2001).
6. G. Plafker, *J. Geophys. Res.* **77**, 901 (1972).
7. S. H. Clarke, G. A. Carver, *Science* **255**, 188 (1992).
8. K. R. Berryman, Y. Ota, A. G. Hull, *Tectonophysics* **163**, 185 (1989).
9. M. Ando, *Tectonophysics* **27**, 119 (1975).
10. For deep-penetration seismic imaging, an air gun array with a large volume ( $\sim 200$  liters) was used as the controlled sound source. Velocity-depth models for the depth migration of reflection data were iteratively constructed by prestack depth migration-velocity analysis (22). Wide-angle data (23) guided the velocity analysis. The final velocity measurement for the depth migration has an  $\sim 10\%$  maximum uncertainty at levels deeper than  $\sim 10$  km.

11. Y. Tanioka, K. Satake, *Geophys. Res. Lett.* **28**, 1075 (2001).
12. M. Kikuchi, Y. Yamanaka, *Seismo* **7**, 6 (2001).
13. Y. Sugiyama, *Geofis. Int.* **33**, 53 (1994).
14. G. F. Moore, T. H. Shipley, *Proc. Ocean Drill. Program. Sci. Results* **131**, 73 (1993).
15. T. H. Shipley, G. F. Moore, N. L. Bangs, J. C. Moore, P. L. Stoffa, *Geology* **22**, 411 (1994).
16. J. Ashi, S. Kuramoto, S. Morita, U. Tsunogai, K. Kameo, *Eos* **82** (fall suppl.), T41A (2001).
17. J. C. Moore, D. Saffer, *Geology* **29**, 183 (2001).
18. M. Hattori, M. Okano, *JAMSTEC J. Deep Sea Res.* **20**, 37 (2002).
19. G. Igarashi et al., *Science* **269**, 60 (1995).
20. R. D. Hyndman, K. Wang, M. Yamano, *J. Geophys. Res.* **100**, 15373 (1995).
21. P. Vrolijk, *Geology* **18**, 703 (1990).
22. Z. Liu, N. Bleistein, *Geophysics* **60**, 142 (1995).
23. A. Nakanishi et al., *J. Geophys. Res.* **107**, EPM 2-1 (2002).
24. A. Asada, K. Okino, *Proc. Jpn. Soc. Mar. Surv. Technol.* **10**, 15 (1998).
25. Bathymetry data were compiled by the Hydrographic Department, Japan Maritime Safety Agency (24).
26. T. Seno, S. Stein, A. E. Gripp, *J. Geophys. Res.* **98**, 17941 (1993).
27. We thank the captain, crew, and technical staff of the R/V *Kairei*. Discussion with the Integrated Ocean Drilling Program Nankai Trough seismogenic zone research group was useful for completion of the initial manuscript.

17 May 2002; accepted 1 July 2002

## Photothermal Imaging of Nanometer-Sized Metal Particles Among Scatterers

David Boyer,<sup>1</sup> Philippe Tamarat,<sup>1</sup> Abdelhamid Maali,<sup>1</sup> Brahim Lounis,<sup>1\*</sup>† Michel Orrit<sup>2\*</sup>

Ambient optical detection of labeled molecules is limited for fluorescent dyes by photobleaching and for semiconducting nanoparticles by "blinking" effects. Because nanometer-sized metal particles do not optically bleach, they may be useful optical labels if suitable detection signals can be found. We demonstrate far-field optical detection of gold colloids down to diameters of 2.5 nanometers with a photothermal method that combines high-frequency modulation and polarization interference contrast. The photothermal image is immune to the effects of scattering background, which limits particle imaging through Rayleigh scattering to diameters larger than 40 nanometers.

An ideal optical label for large molecules should generate an intense optical signal; it should also be small, durable, chemically inert, and apt to bind to the molecule of interest in a controlled manner. All present-day optical markers fall short of the "ideal label" status. The most common labels, fluorescent dyes, can be chemically grafted to the molecule under study. Their redshifted fluorescence can be sifted very efficiently out of the scattering background (1). Their

main drawback, however, is photobleaching, i.e., the irreversible photochemical processes leading from the excited fluorophore to nonfluorescent products. Nanocrystals of II-VI semiconductors (such as CdSe/ZnS) have recently been proposed as optical markers (2, 3). Although they resist bleaching longer than dyes, their luminescence brightness is liable to "blinking" (4), and they are difficult to functionalize in a controlled way.

Metal particles are currently used for single-particle or single-molecule tracking (5) and in immunocytochemistry (6, 7). They include colloids with diameters ranging from a micrometer to a few nanometers, and synthesized clusters (8, 9) with well-defined chemical structures. Submicrometer metal particles down to diameters of 40 nm can be imaged in an optical

<sup>1</sup>Physique Moléculaire Optique et Hertzienne, CNRS et Université Bordeaux I, 351 Cours de la Libération, 33405 Talence Cedex, France. <sup>2</sup>Huygens Laboratory, Universiteit Leiden, Postbus 9504, 2300 RA Leiden, Netherlands.

\*These authors contributed equally to this work.  
†To whom correspondence should be addressed. E-mail: lounis@cpmoh.u-bordeaux.fr

microscope through their Rayleigh scattering by illuminating in dark-field at the plasmon frequency (10), with differential interference contrast (DIC) and video enhancement (11), or with total internal reflection (12). They are very attractive as optical labels because they do not photobleach and do not optically saturate at reasonable exciting intensities. Unfortunately, Rayleigh scattering decreases as the sixth power of diameter, and the scattering signal must be discriminated from a strong background. Therefore, the minimum size of a particle to be detected in a cell or in a scattering tissue is, in practice, well above the limit of 40 nm in diameter. Electron microscopy, with its superior spatial resolution, can distinguish metal particles with diameters as small as 5 nm (13) from cellular organelles, but it does not operate at ambient conditions. The challenge in the present work is to detect such small particles at ambient conditions with an optical microscope. This ability would make it possible to correlate single labels with optical microscopic images, without having to conjugate the label to bulky fluorescent antibodies.

Because the optical absorption of a small metal particle decreases as only the third power of its diameter, absorption will prevail over scattering below a certain size. The absorption cross-section of a gold particle of 5-nm diameter is about  $3 \text{ nm}^2$  at 514 nm (14), which is more than two orders of magnitude greater than that of an organic fluorophore at room temperature. This strong absorption gives rise to a photothermal effect, i.e., an increase in temperature around the particle when it is illuminated by laser light. We have optically detected this temperature change by a sensitive interference method similar to DIC, opening the way to uses of such nanometer-sized metal particles as optical labels. Photothermal detection was proposed previously by Tokeshi *et al.* (15), who used a thermal lens effect to detect very low concentrations of absorbing molecules in liquid solutions. Instead of the thermal lens, we use the very sensitive polarization interference method (16), which allows the detection of slight phase changes induced by heating. We improve noise rejection by means of high-frequency modulation. The volume undergoing temperature modulation is determined by the damping of heat waves at the modulation frequency. The frequency is chosen such that this volume roughly overlaps the focal spot. Photothermal contrast can be implemented with DIC on a standard optical microscope, and this method can be used with organic or biological samples, which will have negligible photothermal background.

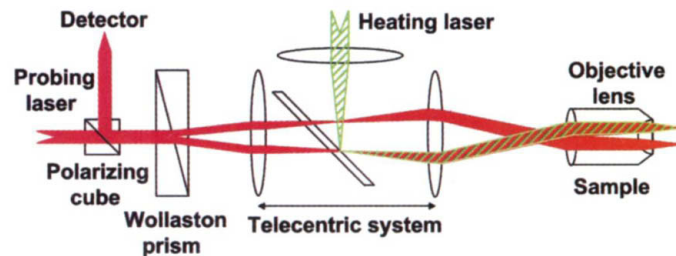
The experiment was performed with two lasers: a (green) argon-ion laser at 514 nm for heating and a (red) helium-neon laser at 633 nm for probing. The green laser had an output of 120 mW, of which a maximum of  $\sim 20 \text{ mW}$

reached the sample. This intensity was modulated at frequencies between 100 kHz and 10 MHz with an acousto-optical modulator. The linearly, horizontally polarized red light was injected by transmission through a polarizing cube (Fig. 1). A Wollaston prism, rotated by  $45^\circ$  from the incident polarization, split the red beam into two orthogonally polarized beams, with a splitting angle of about  $0.1^\circ$ . The two beams were focused in the object plane of the microscope objective ( $\times 100$  magnification; numerical aperture = 0.95, for air) as two diffraction-limited spots,  $1.2 \text{ }\mu\text{m}$  apart. The green beam was superimposed on one of the red beams by a dichroic beam-splitter. For an optimal recombination of the reflected beams in the Wollaston prism (17), we inserted a telecentric lens system to image the Wollaston prism onto the image focal plane of the objective (Fig. 1). The green spot could be moved with respect to the two red ones, and the maximum signal was obtained when it coincided with one of them. As in the usual DIC method, the two beams with orthogonal polarizations recombined in the Wollaston prism. Their phase difference gave rise to a vertically polarized component that was reflected by the polarizing cube and sent to the detector, a fast photodiode, through a red-pass filter that eliminated stray green light. The power at each red spot was  $\sim 2.5 \text{ mW}$ , and the maximum power reaching the photodiode was only about  $150 \text{ }\mu\text{W}$ . We used a lock-in amplifier to detect the variations of the red intensity and thus the dephasing between the two red beams at the modulation frequency of the green beam, with an integration time of 10 ms. Microscopic images were obtained by scanning the sample with respect to the fixed three spots.

The elevation to temperature  $T$  caused at a distance  $r$  of a modulated point source of heat with power  $P [1 + \cos(\omega t)]$  in a homogeneous medium is derived from the equation of heat conduction (18) and is given by

$$T - T_0 = \frac{P}{4\pi\kappa r} [1 + \exp(-r/R)\cos(\omega t - r/R)] \quad (1)$$

**Fig. 1.** Schematic diagram of the optical setup. The horizontally polarized red probing beam is split into two beams by a Wollaston prism and focused on the microscope objective by a telecentric lens system. The reflected beams are recombined in the Wollaston prism, and the vertically polarized beam is reflected and sent to the detector. The green heating beam is modulated at high frequency by an acousto-optical modulator. It induces a periodic phase difference between the two red beams, which gives rise to a modulation of the detected red intensity.



where  $T_0$  is the ambient temperature,  $\kappa$  is the thermal conductivity of the medium, and  $R$  is the characteristic length for heat diffusion at frequency  $\omega$ , given as  $\sqrt{2\kappa/\omega C}$  ( $C$  is the heat capacity of a unit volume of the medium). The phase difference between the two red beams is proportional to the temperature change averaged over the spot size. The signal should be roughly constant for frequencies  $\omega < \omega_s = 2\kappa C^{-1} R_s^{-2}$  (such that  $R$  is larger than the spot size  $R_s$ ) and should decrease for  $\omega > \omega_s$ . Typical values for the heat diffusion constant of organic materials lead to  $\omega_s$  values of  $\sim 1 \text{ MHz}$ .

We prepared the samples by spin-coating, on a microscope cover slip, a drop of an aqueous solution of polyvinyl alcohol (1% by weight) doped with gold nanoparticles. The gold particles had diameters of 20, 10, and 5 nm with half-maximum dispersions in diameters of 2, 1, and 0.6 nm, respectively, according to the manufacturer's specifications. The three-dimensional representation of a photothermal image of 5-nm-diameter gold nanoparticles (Fig. 2A) shows no background scattering from the substrate, which means that the signal arises from the only absorbing objects in the sample, namely, the gold nanospheres. These small nanoparticles are detected with an unusually large signal-to-noise ratio ( $S/N > 10$ ). We were able to image particles with diameters as small as 2.4 nm and with a  $S/N$  of  $\sim 2$ . A histogram of peak heights for about 200 imaged spots (Fig. 2B) shows a fairly narrow unimodal distribution (in good agreement with the manufacturer's specifications), which confirms that the spots stem from individual nanospheres. Stronger peaks that could have been attributed to pairs of particles or to higher order aggregates were rare. We did not find any weaker spots even at a much higher heating power.

We showed that the imaging mechanism is indeed photothermal by determining the dependence of the signal on the particle size and the heating laser power. The signal intensities for 5-, 10-, and 20-nm-diameter spheres varied linearly with the volume of the particles. The signal is perfectly linear in heating power with no sign of saturation in the range of intensities

used in the present experiments (up to 20 MW/cm<sup>2</sup> for the smallest spheres). A rough calculation of the temperature increase of the 5-nm spheres at this power gives about 15 K at the surface of the sphere, a temperature increase for which we expect no appreciable change in optical properties.

We then investigated how the signal intensity depends on the distance between the green and red spots. When we moved the green spot

away from the two red ones, the signal decreased smoothly with distance, which rules out purely local effects of the green spot. Equation 1 predicts a signal decreasing as the inverse square of the distance, at large enough distances. The decrease we observed was indeed steeper than  $1/r$ , although the distance range was too narrow to determine the exponent. As expected, the signal is largest when the green spot overlapped one of the red spots (Fig. 3A) and pre-

sented a dispersion-like shape when the green spot was exactly in the middle of the red ones (Fig. 3B). In addition, the signal showed the expected decrease with modulation frequency (Fig. 3C), in agreement with numerical simulations based on heat diffusion.

For future applications of photothermal imaging in single-particle tracking or for the localization of labeled biomolecules, the effect of scattering on the photothermal image must be considered. For this purpose, we added large latex spheres as well-calibrated scatterers to the spin-coating solution. Figure 4 shows images of a sample containing three types of particles: latex spheres with 300-nm diameter, gold spheres with 80-nm diameter, and gold nanoparticles with 10-nm diameter. The DIC image (Fig. 4A) shows scattering and absorbing structures. The latex spheres, which are very strong scatterers, gave intense signals with positive and negative contrast. The 80-nm absorbing gold spheres appeared with negative contrast on the image, but their intensity is much weaker than that of the latex spheres. In the photothermal image where a very low heating power (<100  $\mu$ W) was used (Fig. 4B), the 80-nm gold spheres appear at the same location as in the DIC image. When we increased the heating power to 5 mW (Fig. 4C), those particles gave very intense signals that saturated the lock-in amplifier. The spots from the 10-nm particles appeared very clearly in this high-power image. In both photothermal images, the latex spheres were completely absent. Our photothermal method is totally insensitive to non-absorbing scatterers, even when they are large objects with strong index contrasts with their surroundings. Only absorbing objects with high saturation intensities will appear in the photothermal image under our present conditions. In biological samples in particular, the absorption background from fluorescent labeling or from absorbing biomolecules would be negligible.

The photothermal detection of small absorbing labels has distinct advantages over fluorescence detection. The method is free of background noise, even in scattering environments. There is neither photobleaching, nor saturation for illumination intensities up to several tens of MW/cm<sup>2</sup>. To our knowledge, no other optical method, not even near-field optics (19), is able to detect nonfluorescing objects as small as 2.5 nm. This represents a gain of more than three orders of magnitude in volume over the current optical detection by plasmon Rayleigh scattering. The photothermal method could be applied to many diffusion and colocalization problems in physical chemistry and materials science, and in cellular biology, to track labeled biomolecules in living cells. Plasmon resonances of nanoparticles shift according to metal composition, particle size, and surroundings and could be exploited for color-dependent imaging. All

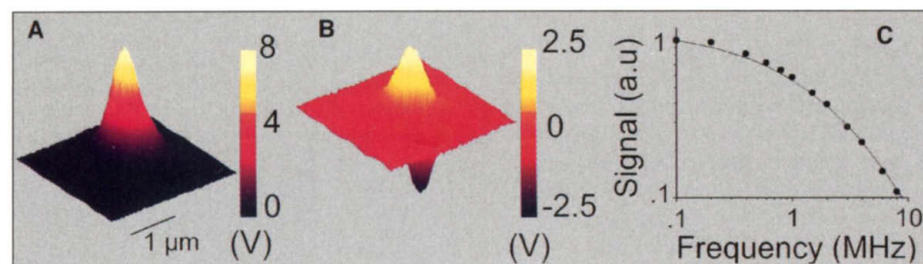
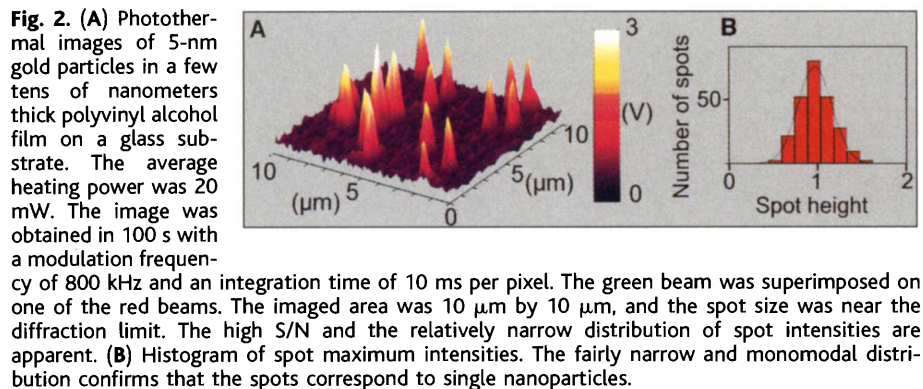


**Fig. 3.** (A and B) Images of a 2.4  $\mu$ m by 2.4  $\mu$ m sample area with a 20-nm-diameter gold nanoparticle for two relative positions of the green spot with respect to the red ones: superimposed on one of the red spots (A) and in the middle of the red spots (B). (C) The signal as a function of the modulation frequency when the green spot is on one of the red spots. The curve is correctly fitted by a numerical simulation based on heat diffusion.

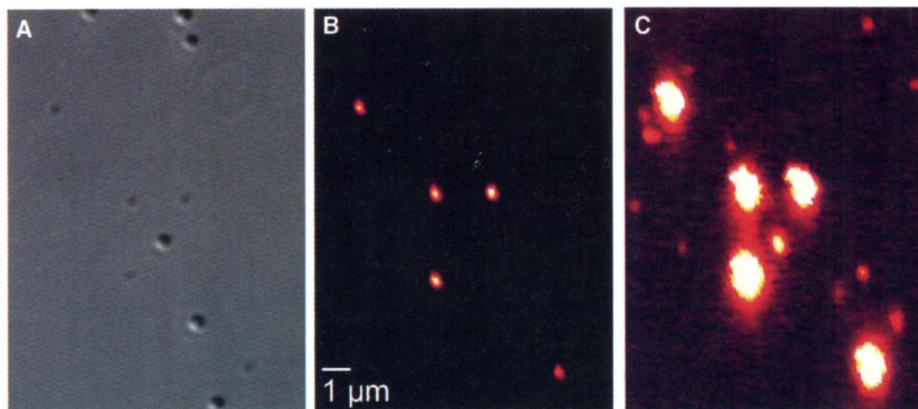


**Fig. 4.** (A) Differential interference contrast and (B and C) photothermal images of a sample containing 300-nm-diameter latex spheres, 80-nm-diameter gold spheres, and 10-nm-diameter gold spheres. The heating intensity was 30 kW/cm<sup>2</sup> (B) or 1.5 MW/cm<sup>2</sup> (C). The 80-nm gold spheres appear on all three images and allowed direct comparisons of the same imaged sample area. In the DIC image, the 10-nm particles are not visible, whereas the 300-nm latex spheres give very strong signals and the 80-nm gold spheres give weaker ones. In (B), a photothermal image at low power shows only the large metal particles. In (C), at high heating power, the 10-nm particles are clearly visible, whereas the 80-nm gold spheres saturate the detection capability. The strongly scattering latex spheres are completely absent in the photothermal images.

these features would enable true single-molecule measurements over arbitrarily long times.

In this work, we have estimated the temperature rise of metal particles 5 nm in diameter at about 15 K. The temperature rise declines as the reciprocal distance from the particle's center, decreasing to 3 K at a distance of 13 nm from the center. Although small, this temperature increase might still be too high for some proteins or biomolecules. We believe, however, that the S/N can be substantially improved in a transmission geometry and by reaching the photon noise limit in detecting the probe beams. The label heating could then be reduced by a factor of 10 and would become negligible for most biomolecules at ambient conditions.

## Electron Solvation in Two Dimensions

A. D. Miller,<sup>1</sup> I. Bezel,<sup>2</sup> K. J. Gaffney,<sup>1\*</sup> S. Garrett-Roe,<sup>1</sup> S. H. Liu,<sup>1</sup> P. Szymanski,<sup>1</sup> C. B. Harris<sup>1†</sup>

Ultrafast two-photon photoemission has been used to study electron solvation at two-dimensional metal/polar-adsorbate interfaces. The molecular motion that causes the excess electron solvation is manifested as a dynamic shift in the electronic energy. Although the initially excited electron is delocalized in the plane of the interface, interactions with the adsorbate can lead to its localization. A method for determining the spatial extent of the localized electron in the plane of the interface has been developed. This spatial extent was measured to be on the order of a single adsorbate molecule.

The interaction of excess electrons at interfaces is not only of fundamental interest, but affects processes such as charge injection and transport in molecular electronics and electrochemistry (1, 2). Electron solvation represents a general interaction of an electron with its surroundings. In the broadest sense, electron solvation occurs when the molecules surrounding an electron reorganize to accommodate the electron's charge density. Although extensive investigations of solvation in isotropic media have been conducted (3–7), comparatively little is known about the dynamics of electron solvation at metal/molecular interfaces. Both the reduced dimensionality and hindered solvent motion could lead to dynamics distinct from those of isotropic materials (8–11).

### References and Notes

- W. E. Moerner, M. Orrit, *Science* **283**, 1670 (1999).
- M. Bruchez Jr., M. Moronne, P. Gin, S. Weiss, A. P. Alivisatos, *Science* **281**, 2013 (1998).
- W. C. Chan, S. Nie, *Science* **281**, 2016 (1998).
- M. Nirmal et al., *Nature* **383**, 802 (1996).
- M. P. Sheetz, S. Turney, H. Qian, E. L. Elson, *Nature* **340**, 284 (1989).
- W. Baschong, J. M. Lucocq, J. Roth, *Histochemistry* **83**, 409 (1985).
- J. W. Slot, H. J. Geuze, *Eur. J. Cell Biol.* **38**, 87 (1985).
- P. A. Frey, T. G. Frey, *J. Struct. Biol.* **127**, 94 (1999).
- J. F. Hainfeld, R. D. Powell, *J. Histochem. Cytochem.* **48**, 471 (2000).
- S. Schultz, D. R. Smith, J. J. Mock, D. A. Schultz, *Proc. Natl. Acad. Sci. U.S.A.* **97**, 996 (2000).
- J. Gelles, B. J. Schnapp, M. P. Sheetz, *Nature* **331**, 450 (1988).
- C. Sönnichsen et al., *Appl. Phys. Lett.* **77**, 2949 (2000).
- J. M. Robinson, T. Takizawa, D. D. Vandre, *J. Microsc.* **199**, 163 (2000).
- C. F. Bohren, D. R. Huffman, *Absorption and Scattering of Light by Small Particles* (Wiley, New York, 1983).
- M. Tokeshi, M. Uchida, A. Hibara, T. Sawada, T. Kitamori, *Anal. Chem.* **73**, 2112 (2001).
- P. Cleyzes, A. C. Boccarda, H. Saint-Jalmes, *Opt. Lett.* **22**, 1529 (1997).
- If cells or other bulk samples were studied, the two transmitted red beams would have to recombine in a second Wollaston prism. Here, to demonstrate photothermal detection of metal particles on surfaces, we used the weaker beams reflected by the glass substrate at the expense of the final signal and S/N ratio.
- H. S. Carslaw, J. C. Jaeger, *Conduction of Heat in Solids* (Oxford Univ. Press, Oxford, ed. 2, 1986).
- T. Klar et al., *Phys. Rev. Lett.* **80**, 4249 (1998).
- We thank D. Choquet for helpful discussions, L. Cognet for valuable help with the DIC setup, and J.-M. Turllet for various equipment. Funding of this work by CNRS (Individual Nano-Object program), Région Aquitaine, and the French Ministry for Education and Research (MENRT) is gratefully acknowledged.

9 May 2002; accepted 8 July 2002

trons photoexcited to states delocalized in the plane of the interface to localize if the solvent dipole-layer distortion leads to the formation of an energetically favorable site.

We used TPPE to investigate electron solvation and the resulting localization dynamics on acetonitrile/Ag(111) and butyronitrile/Ag(111) interfaces. The instrument function of the laser at the 1.7 to 1.9 eV probe and the 3.4 to 3.8 eV second-harmonic pump photon energies used was  $\sim 100$  fs. The two nitriles have molecular dipole moments of 3.9 and 3.7 Debye, respectively (17, 18). The layer-by-layer growth of the nitriles on the Ag(111) surface has been confirmed with TPPE, which produced distinctly different spectra for monolayer and bilayer coverages. The layers were adsorbed at temperatures between 100 and 140 K, and the data was collected at a temperature of 80 to 90 K. Electrons in polar molecular glasses still solvate at these temperatures, though on a longer time scale (19). Low-energy electron diffraction (LEED) studies of these interfaces lack LEED spots, demonstrating the absence of long-range translational order. Similar conclusions have been drawn from near edge x-ray absorption fine structure experiments for acetonitrile adsorbed on Ag(110) (20) and Au(100) (21) and LEED experiments on acetonitrile/Au(100) (22). Acetonitrile has a negative electron affinity of  $-2.8$  eV (23), indicating that the image potential state electrons should be pushed out to the layer/vacuum interface and not interact with the electronic structure of the layer.

TPPE was used to populate the electron's image potential states and observe their subsequent dynamics. Image potential states result from the attractive interaction between an electron outside of a surface and the surface polarization that it induces. The resultant Coulomb potential supports an infinite series of hydrogenic states confined normal to the surface (13, 24, 25). Parallel to the surface,

<sup>1</sup>Department of Chemistry, University of California, Berkeley, and Chemical Sciences Division, E. O. Lawrence Berkeley National Laboratory, Berkeley, CA 94720, USA. <sup>2</sup>Miller Institute for Basic Research in Science, 2536 Channing Way #5190, Berkeley, CA 94720, USA.

\*Present address: Department of Chemistry, Stanford University, Stanford, CA 94305, USA.

†To whom correspondence should be addressed. E-mail: harris@socrates.berkeley.edu